AN ANCIENT CHINESE BRONZE FRAGMENT RE-EXAMINED AFTER 50 YEARS: CONTRIBUTIONS FROM MODERN AND TRADITIONAL TECHNIQUES*

M. L. YOUNG,[1] F. CASADIO,[2]† J. MARVIN,[1] W. T. CHASE[3] and D. C. DUNAND[1]

[1]*Department of Materials Science and Engineering, Northwestern University, Evanston, IL 60208, USA*
[2]*The Art Institute of Chicago, Chicago, IL 60603, USA*
[3]*Chase Art Services, 508 Route 169, Woodstock, CT 06281, USA*

Modern analytical techniques, such as secondary ion mass spectrometry, inductively coupled plasma optical emission spectroscopy, in-situ *synchrotron X-ray diffraction and Raman microscopy, alongside scanning electron microscopy with energy-dispersive X-ray analysis and powder X-ray diffraction, were used to investigate bronze fragments from an ancient Chinese bronze vessel (also known as a* hu*) in the collection of the Art Institute of Chicago. Previous compositional results obtained by R. J. Gettens in 1951, using traditional optical metallography and powder X-ray diffraction, were compared with the present analysis. The investigation provided a complete description of the composition of the ancient metal alloy and spatially resolved identification of the major and minor corrosion products. Furthermore, the study also provided the opportunity for a better understanding of the possibilities and limitations of the various instrumental techniques available to the analyst for the study of ancient bronzes.*

KEYWORDS: SIMS, ARCHAEOMETALLURGY, RAMAN MICROSCOPY, SYNCHROTRON RADIATION (SR)-XRD, ICP–OES, CHINESE BRONZES

INTRODUCTION

Beyond written sources, the study of ancient civilizations often relies on the investigation of their utilitarian and decorative artefacts. This methodological approach is relevant to one of the highest achievements of ancient China: bronze technology. Extensive scientific archaeological excavations in China have brought to light a profusion of bronze vessels and artefacts traceable to a known context and, as a result, the knowledge accumulated on ancient Chinese bronzes has greatly increased in the last 50 years (Bagley 1980, 1987, 2001; Rawson 1990; Linduff *et al.* 2000; Thorp 2005; von Falkenhausen 2006). At the same time, the techniques available to investigate ancient bronzes have greatly improved as compared to the simple, albeit effective, tools of metallography and X-ray diffraction (XRD) available half a century ago.

In this research, several bronze fragments (known as the 'Kelley bronze' fragments) from an ancient Chinese vessel (*hu*) in the collection of the Art Institute of Chicago (Illinois, USA) were subjected to a series of tests based on modern analytical techniques. The present paper presents results from this new analytical campaign involving the use of traditional techniques (optical microscopy and powder XRD) together with a battery of modern analytical techniques, including secondary ion mass spectrometry (SIMS), inductively coupled plasma optical emission spectroscopy (ICP–OES), Raman microscopy, scanning electron microscopy/energy-dispersive X-ray

Figure 1   *An ancient Chinese bronze vessel (*hu*) very similar to the 'Kelley' bronze vessel (*hu*). This photograph, from Gettens' original notes, was long assumed to have been taken from the 'Kelley' bronze vessel. (See online for a colour version of this figure.)*

analysis (SEM/EDX) and electron microprobe, which provided a complete, spatially resolved description of the complex layering of corrosion products and the bulk metal both at the elemental and molecular level. Results from a separate study using high-energy synchrotron X-ray diffraction (SR-XRD) (Young *et al.* 2006), on the same region where samples have been removed from the fragment for the present study, are also summarized to evaluate a non-destructive method for the study of ancient metallic artefacts.

HISTORICAL CONTEXT

The photograph in Figure 1 of an ancient Chinese vessel (*hu*) originally came from Gettens' notes (detailed below) and has long been assumed to have been taken from the original, intact 'Kelley' bronze. Purchased as a collectible from China, the vessel broke into pieces during shipping to the United States in the mid-1940s, revealing it as a collection of fragments (Figs 2 and 3). The original fragments had been soft-soldered to new replacement pieces made from copper plates used to fill missing fragments (Fig. 3 (b)). The surface of the replacement pieces was then covered with artificial patina and missing decorative elements were re-created in order to camouflage the partial forgery. This vessel is of particular interest, since both an authentic patina, accumulated over centuries of burial, and a 19th or early 20th century artificial patina coexist on adjacent areas, as
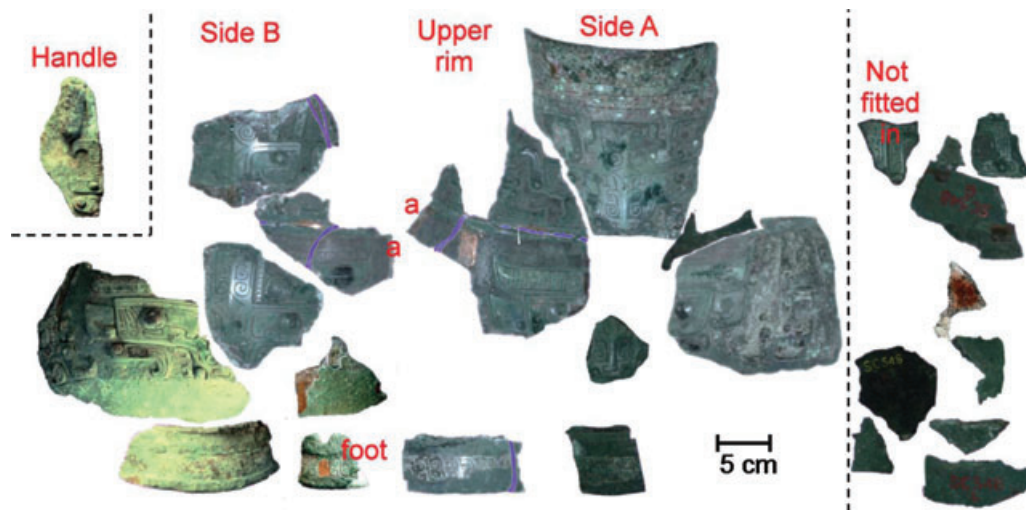
Figure 2   *A compilation of photographs of 11 of the 'Kelley' bronze fragments from an ancient Chinese bronze vessel* (hu) *in a provisional restoration. Only one fragment shows the upper rim. Two masks appear on each side of the vessel; the eyes of the lower masks have a delineated pupil. Three bowstrings appear just down from the upper rim, and the clear band separating the two masks vertically is also present, though fragmentary. The variations in colour and contrast are due to differences in the original photographs. The AIC fragments are shown on the left-hand side. (See online for a colour version of this figure.)*
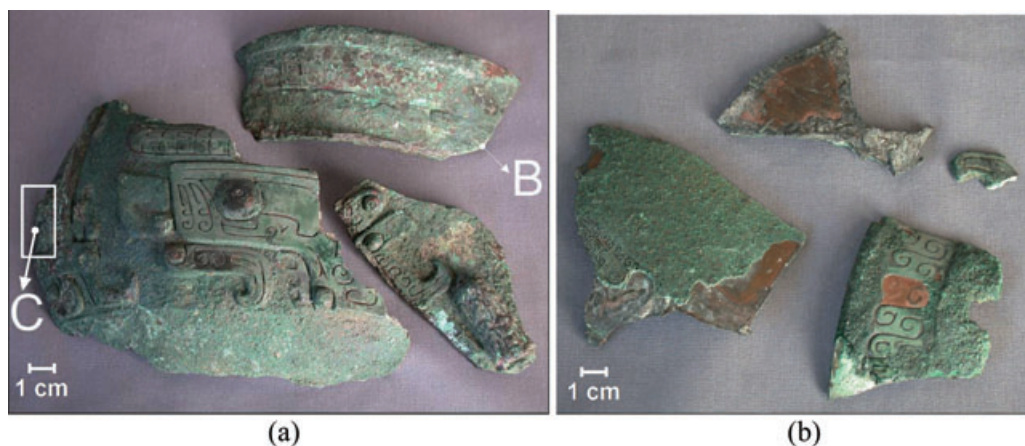

Figure 3   *(a) The 'Kelley' bronze fragments studied here, from an ancient Chinese bronze vessel* (hu). *The white letters (B and C) indicate sample locations. The area framed by the white rectangle on the largest fragment is the location where* in-situ *SR-XRD was performed. (b) Modern copper plates with applied patina used to compensate for missing fragments on the ancient Chinese vessel. (Photographs courtesy of S. R. Schnepp, Conservation Department, The Art Institute of Chicago; see online for a colour version of this figure.)*

observed by Gettens (1951, 1969). Upon arrival in the United States, the fragments were dispersed. Archival research based on the Art Institute of Chicago registrar's records, publications by Gettens (1951, 1969), and the unpublished diary of Charles Fabens Kelley (1885–1960, the curator of Asian Art at the Art Institute of Chicago at the time) indicate that Mr Irvin S. Layton of Boise City

(Oklahoma) shipped an unknown number of fragments of this vessel to the Art Institute as a personal gift to Mr Kelley, who received them on 9 September 1946 (recorded in the museum's collection database with the unique identifier of 'R of O 10478'), was much impressed by the quality of the shattered vessel fragments (E. L. Pearlstein, Art Institute of Chicago, pers. comm.) and attributed the vessel to 'the Zhou period (1112–255 B.C.)' (Gettens 1951, 1969). Kelley brought four of these fragments to Rutherford J. Gettens (1900–74), the scientific conservator at the Fogg Art Museum, Harvard University and founding Director of the Technical Laboratory, Freer Gallery of Art, Smithsonian Institution, during his visit to Cambridge, Massachusetts in October 1946, and shipped additional pieces to Gettens on 27 November (AIC shipping order 38969). Later, Gettens described his scientific analyses of cross-sections of the fragments by optical metallography, powder XRD and spectroscopy, thus identifying the bulk metal to be a Cu–Sn alloy composed of 72–74 wt% Cu, 20–22 wt% Sn and 4.1–4.6 wt% Pb (Gettens 1951, 1969). Gettens characterized the majority of the corrosion products; however, he was unable to identify all of them using the techniques available at the time.

In the course of this investigation, it was possible to use digital photography to bring together the pieces housed in the Art Institute of Chicago with the ones housed at the Freer and Sackler Galleries. Figure 2 shows a virtual restoration of the bronze vessel, illustrated here for the first time. Careful examination of the partially reconstructed vessel shown in Figure 2 indicates that it is similar but not identical to the *hu* shown in Figure 1. For example, the central forehead and nose on the upper mask on the 'Kelley' bronze (directly under 'Side A' in Fig. 2) has small protruding elements on each side; these are absent in Figure 1. Also, the decoration on the foot of the 'Kelley' bronze is squared spirals with protruding elements at the corners. The decoration on the foot of Figure 1 is a plainer spiral, more like the common *lei-wen* spirals. The original source of the photograph shown in Figure 1 has been lost, but even though it does not show the 'Kelley' bronze, it does give a valuable clue as to the actual shape of the 'Kelley' bronze—a flattened oval. Perhaps, in the future, all the fragments can be brought together in one place and assembled, photographed and dispersed again.

To better understand the discussion below, a brief description of early Chinese chronology is necessary. The exact chronology of the three early dynastic periods (Xia, Shang and Zhou) is still controversial. Current scholarship suggests that the Xia Period spanned from *c.* 2100 BC to 1600 BC, the Shang Period spanned from *c.* 1600 BC to 1046 BC and the Zhou Period spanned from 1046 BC to 221 BC (Loewe and Shaughnessy 1999; Xueqin 2002; Rawson 2009). The late Shang Period (*c.* 1300 BC to 1046 BC) is further divided into four parts; Anyang Period II (the time of Fu Hao) will be mentioned below (Jin *et al.* 1998a). The Zhou Period is further divided into two parts; Western Zhou (1046 BC to 771 BC) and Eastern Zhou (770 BC to 221 BC), which is also further subdivided, with the relevant period to our discussion being the Warring States (403 BC to 221 BC).

EXPERIMENTAL PROCEDURES

Metallography

As shown in Figure 3 (a), two samples (labelled B and C) were sectioned from two different bronze fragments for investigation after careful visual, stereomicroscopic and UV light observations. Furthermore, X-ray radiographic images of the fragments were carefully studied to ascertain that samples were taken from original portions of the vessel. Sample B (part of the foot of the vessel) and sample C (part of the body of the vessel) were separately mounted in epoxy resin and prepared for metallographic study. These mounted samples were then polished in successive

steps using silicon carbide grinding pads (180, 320, 400 and 600 grit) with water and diamond water-based suspensions (9, 3 and 1 μm) on a microcloth pad for the final polish. SEM/EDX was performed on cross-sections B and C using a Hitachi S-3500N variable-pressure SEM operated at 12 kV.

Micro-Raman spectroscopic analysis

Micro-Raman spectroscopy was performed directly on polished cross-sections of samples B and C with a Horiba Jobin-Yvon Labram 300 confocal Raman microscope, equipped with a multi-channel air-cooled open electrode charge-coupled device (CCD) detector (1024×256), a holographic notch filter and a dispersive grating with 1800 grooves per millimetre. The excitation line of an air-cooled frequency-doubled Nd:Yag solid state laser ($\lambda_0 = 532$ nm) was focused through a 100× Olympus objective on to the samples and Raman scattering was back-collected through the same microscope objective. Laser power on the samples was kept very low (never exceeding a few mW) by a series of neutral density filters in order to avoid any thermal damage.

Micro-Fourier transform infrared spectroscopic analysis

Micro-Fourier transform infrared (FTIR) spectroscopy of a small flake of the fake patina removed from the bronze fragment was performed using a Bruker Tensor 27 FTIR spectrophotometer with mid-IR glowbar source and Hyperion 2000 Automated FTIR microscope with nitrogen cooled mid-band and broad-band MCT detectors. Samples were analysed in transmission through the microscope after compression in a diamond micro-compression cell, at a resolution of 4 cm^{-1}.

Synchrotron radiation X-ray diffraction analysis

High-energy X-ray diffraction measurements were carried out at the Advanced Photon Source (Argonne National Laboratory, IL), using a monochromatic 85 keV ($\lambda = 0.015$ nm) X-ray beam with a cross-section of 20×200 μm^2 for exposure times of approximately 60 s. The largest bronze vessel fragment (from which sample C was excised) was positioned with its vertical face at a 30° angle relative to the beam. An on-line image plate (345 mm diameter, 100 μm pixel size and 16-bit dynamic range) was used to record complete Debye–Scherrer diffraction cones from the crystalline phases present in the diffraction volume, as well as from ceria powder, which was placed on the back surface of the bronze fragment for calibration purposes. The sample-to-detector distance was 500 mm. The software programs Matlab and Jade were used to create intensity versus *d*-spacing graphs and for phase identification, respectively. The general set-up for these experiments is the same as that described in Young *et al.* (2006) and is similar to that described in Newbury *et al.* (2004, 2006) and Stephenson *et al.* (2001).

Secondary ion mass spectrometry analysis

SIMS was performed on a polished cross-section of sample C. A highly polished surface is needed to obtain sharp elemental, spectral peaks, which aids in the distinction from the background and also helps to avoid overlapping peaks. The instrument used was a static SIMS–PHI TRIFT III (Physical Electronics), using a pulsed primary Ga$^+$ ion beam with an energy of 15 keV and a very low current density allowing for the outermost surface (~0.5 nm) of the specimen to be probed. Typically, the primary ion dose is $<10^{12}$ ions cm^{-2} for mass analysis and $<10^{13}$ ions

cm^{-2} for imaging. Before each SIMS scan, the selected area was sputtered using a 200×200 μm^2 beam for 20 s to remove the surface layer and any impurities from polishing. A test scan was performed for 1 min before each scan to verify instrument accuracy and to achieve a clean surface. Once the measurement scan was started, no adjustments were made to the instrument. All scans were performed using a 100×100 μm^2 beam for 12 min each. Five different areas of the bronze sample were scanned. Before and after scans of the bronze sample, one to three different areas of a polished lead standard (NIST SRM 981) mounted next to the sample were scanned to verify instrument accuracy. The use of a standard with known isotope ratios allows for absolute measurements of isotope ratios in the sample after performing a calibration calculation.

The peaks for the four main Pb isotopes (^{204}Pb, ^{206}Pb, ^{207}Pb and ^{208}Pb) were measured. The measuring range was approximately 0.3 in atomic mass for each spectral peak. The background was taken from atomic mass regions 202.85–203.15 and 208.85–209.15, where no other spectral peaks were observed, averaged and subtracted from the spectral peak areas. After background subtraction, a small ^{209}Pb peak was observed, despite the lack of a Pb isotope with that mass. It was assumed that this peak consisted of ^{208}Pb + ^{1}H cluster. Counts from this peak were thus added to those for the ^{208}Pb peak. It was assumed that all other isotopes showed similar 'spillage' with the same ratio as for ^{209}Pb/^{208}Pb, and corrections were made accordingly for all peaks. For instance, for ^{208}Pb, 2747 ions were added from the spillage to the ^{209}Pb peak (as ^{208}Pb + ^{1}H), and 1075 ions were subtracted, as they belong to ^{207}Pb + ^{1}H.

Inductively coupled plasma atomic emission spectroscopy

ICP–OES was performed at the Analytical Services Laboratory (ASL) at Northwestern University (NU) using a Varian model ICP spectrometer with spectral range from 175 to 785 nm and resolutions of 0.008, 0.015 and 0.040 nm at 160–335, 335–670 and 670–850 nm, respectively. A sample of approximately 10 mg of bulk material was collected by drilling a small hole (diameter: 1/16 in using cobalt steel drill bits) in the largest bronze fragment in the same place, where sample C was excised. Additional standard samples from commercial bronzes (copper alloys: 83300, 84400 and 85200 from SIPI Metals Corporation; 90300, 93200 and 93700 from Atlas Bronze; and 1107, 1110, 1112 and 1115 from NIST) with similar compositions to the ancient bronze sample were also collected using the same methodology. The samples were then diluted to approximately 5, 10, 20, 100 and 200 ppm in ~3% aqua regia. To each dilution, 1 ppm of Eu was added as an internal standard for ICP–OES. In addition to an internal standard, ICP–OES standards were also created for each selected element (As, Bi, Cr, Cu, Fe, Ni, Pb, Sb, Sn and Zn). Each set of ICP–OES standards consisted of 0.1, 0.5, 1, 5, 10 and 25 ppm concentration of each element present. A blank consisting of 3% HNO$_3$ was also created to provide a background subtraction for a concentration of 0 ppm.

RESULTS AND DISCUSSION

UV light, metallography, SEM/EDX, Raman and FTIR spectroscopy

As observed by Gettens (1951, 1969), both an authentic patina, accumulated over centuries of burial, and a 19th or early 20th century artificial patina, which coexist on adjacent areas, can be clearly seen in Figure 4, where ultraviolet (UV) light illumination causes orange auto-fluorescence of the binder used to apply the fake patina.

Figure 4 *A photograph under ultraviolet (UV) illumination of the largest bronze fragment. Orange fluorescence, caused by the natural resin used as an adhesive for the fake corrosion, indicates the artificial patina. (Photo courtesy of S. R. Schnepp, Conservation Department, The Art Institute of Chicago; see online for a colour version.)*

Although SEM/EDX is useful in providing visualization of the microstructure and elemental information about the corrosion products and the bulk metal, it is significantly more powerful when coupled with other techniques such as Raman and FTIR as shown here. A line scan performed on the cross-sections with the Raman microscope allowed for the molecular speciation and depth-profiling of the corrosion products whose elemental distribution was visualized in SEM/EDX maps. Additionally, Raman microscopy performed in parallel with optical micro-scopy allowed direct correlation of chemical composition with the observed colours of corrosion layers. The following paragraphs highlight the results from these techniques applied to cross-sections of samples B and C from the bronze fragment in Figure 3 (a), where sample B (a cross-section of which is shown in Fig. 13) is significantly more corroded than sample C (a cross-section of which is shown in Fig. 5 at three different magnifications).

Outer wall of sample C Figures 6 (a)–(c) show elemental SEM maps of three areas from sample C corresponding to a cross-section from the body of the original vessel (Fig. 5). The corrosion phenomena can be divided in three principal areas proceeding outwards from the bulk of the metal to the outer wall of sample C: (a) an interpenetration zone, (b) a corrosion band and (c) an outer layer characterized by the build-up of porous corrosion products; the latter also includes elements, such as Si and Cl, foreign to the bronze and derived from the burial soil.

As illustrated in Figure 6 (a), X-ray maps of the bulk of sample C reveal Cu-rich dendrites in a Cu–Sn matrix with small Pb inclusions measuring 5–10 μm. Although the bulk of this sample appears uncorroded, corrosion is visible in the interpenetration zone, preferentially attacking the matrix phase (Figs 6 (a) and 6 (b)). The Cu dendrites near the surface are completely corroded and the corrosion band, illustrated in Figure 6 (b), shows accumulation of Sn corrosion products with interdispersed Pb corrosion products. As described more extensively later, Raman micro-
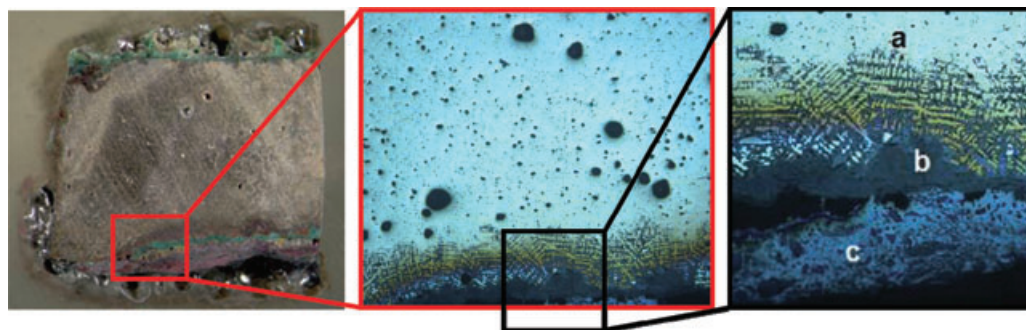
Figure 5   *Optical images of sample C at three different magnifications, showing a porous metal core with layered regions of corrosion products (a, b and c) related to the outer wall. (See online for a colour version of this figure.)*

scopy also highlighted the presence of a cuprite (Cu_2O) layer and increased concentration of copper chlorides at the interface between the corrosion band and the metal. The presence of a cuprite layer associated with intergranular corrosion can be used as an indicator that the patina is authentic and has not been artificially produced (Eichhorn 1988). In the outermost porous corrosion layer (Fig. 6 (c)), the widespread presence of Cl and significant amounts of angular Si-rich particles, presumably quartz (SiO_2) grains, are observed, together with a localized corrosion band rich in Sn and Pb.

Chlorine distribution in the 'Kelley' bronze was previously studied in detail at the Freer Gallery of Art and at the National Institute for Standards and Technology, where samples similar to the Art Institute of Chicago samples were taken from a foot fragment in the Freer Gallery of Art Study Collection (SC-B-18), mounted as cross-sections and examined using traditional metallography (Gettens 1951, 1969). In this previous study, it was found that chlorine, commonly found in salts in excavation sites, plays a significant role in the formation of many of the corrosion products. To extend this previous research, an area at the interface of the corrosion and solid metal, similar to that shown just under 'a' in Figure 5, was chosen for investigation with electron microprobe. Conditions were like the lower left part of Figure 6 (a), where the front of corrosion penetration can be easily seen. Chlorine was clearly detected in the corroded portion of the bronze and area mapping allowed for visualization of the association of chlorine with the corrosion front. An area map showing concentrations of chlorine (red), copper (green) and tin (blue) is shown in Figure 7, along with a line scan. The scans confirmed the presence of chlorine at the spots where corrosion was beginning in the interior of the 'Kelley' bronze, with levels detected through spot analysis ranging from 3 wt% up to 10–11 wt% Cl.

The microstructure and its characteristic elemental distribution depicted in Figures 6 and 7, as well as the loss of shape of the original surface, are consistent with the well-known phenomenon of Type I corrosion (Chase 1994; McCann *et al.* 1999). This form of natural weathering involves volumetric changes at the corrosion interface and preferential corrosion of Sn from the δ phase (67 wt% Cu) in the α + δ eutectoid to form either Sn oxide or mixed Sn and Cu oxides at the surface. This mechanism typically leaves behind the α phase (~90 wt% Cu), which is more corrosion resistant in the alkaline and reducing conditions typically found in Chinese deep tombs (Pelton 2006; Chase *et al.* 2007). The electrochemistry of this process is driven by anionic control, involving migration of Cl^- ions from the environment deep into the bronze (Robbiola *et al.* 1998), a phenomenon confirmed by electron microprobe analysis (Fig. 7).
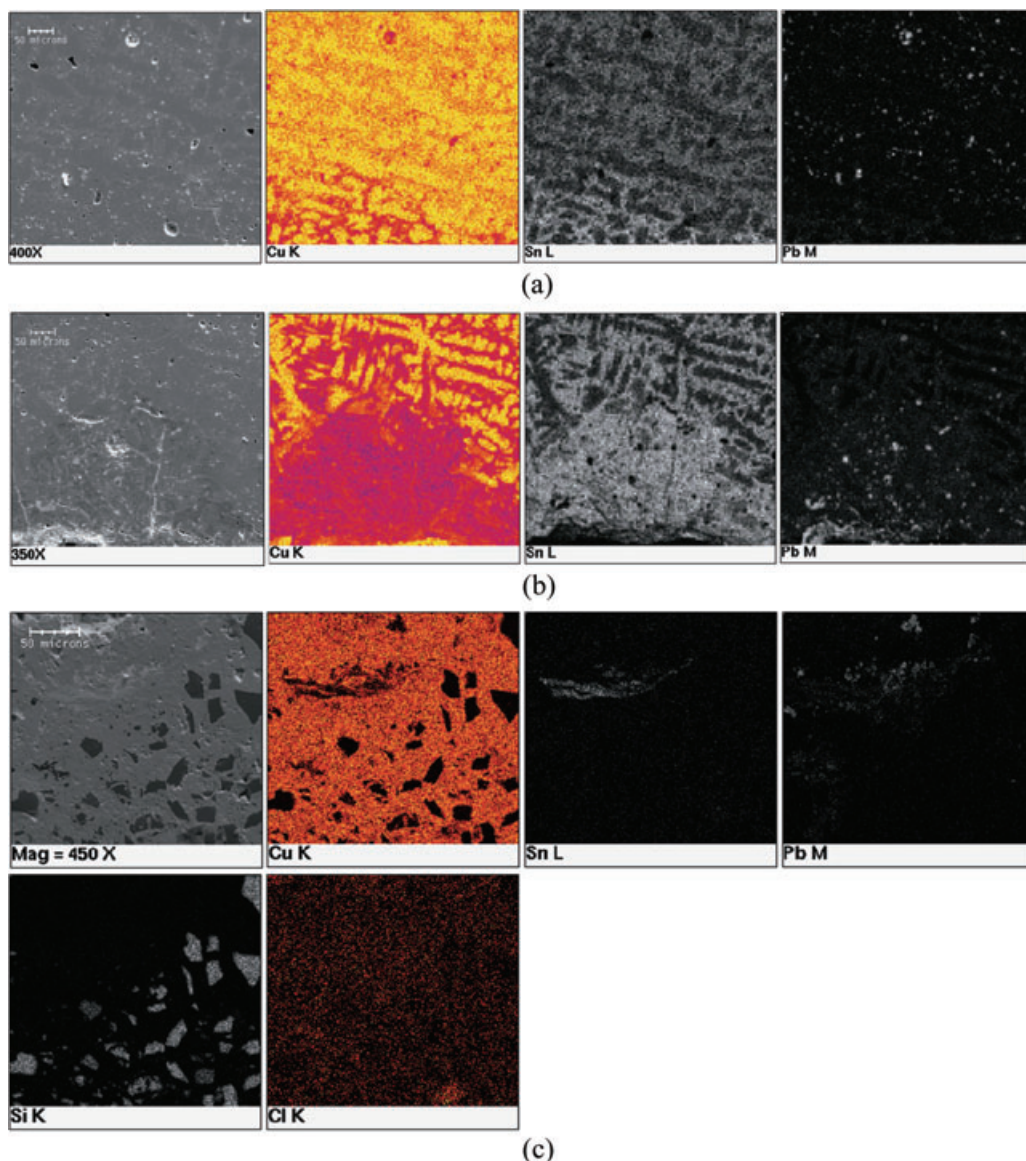
Figure 6 *SEM images and elemental distribution maps from the outer wall of sample C from the bronze fragment. Three areas from the bulk of the metal to the outer wall are observed: (a) an interpenetration zone, (b) a corrosion band, and (c) an outer layer of porous corrosion products as labelled in the optical image in Figure 5. (See online for a colour version of this figure.)*

Figure 8 shows the chemical composition of the various corrosion layers, as detected by Raman microscopy on the outer side of sample C, with spectra collected from positions shown in the optical image in Figure 9. Starting at the bulk of the metal and progressing outwards, several sub-regions (a–f) are observed and their composition identified as follows: (a) in the interpenetration zone, copper sulphide (Cu_2S) was identified in the dark regions of corroded
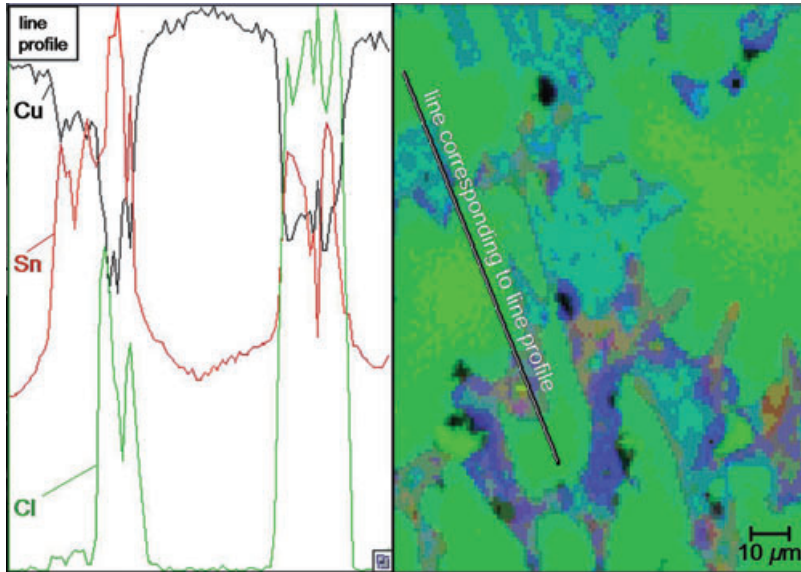
Figure 7   *An elemental analysis map and line scan for chlorine (red), copper (green) and tin (blue) on a cross-section from the foot of the 'Kelley' bronze vessel. The lens-shaped area of the $\alpha + \delta$ eutectoid at the upper left is uncorroded, but the corrosion front has penetrated to the lower right and chlorine is sufficient here to show a purple tone. From the left, the regions traversed in the line scan are alpha, $\alpha + \delta$ eutectoid, the corrosion front (with high tin and chlorine), alpha, another (thicker) corroded area and then more alpha. (See online for a colour version of this figure.)*

eutectic around the Cu dendrites (McCann *et al.* 1999); (b) in the corrosion zone, cuprite (Cu_2O) and anglesite ($PbSO_4$) were identified in the red corrosion band adjacent to the dendrites; (c) in the corrosion zone, atacamite ($CuCl_2 \cdot 3Cu(OH)_2$) and $PbSO_4$ were detected in the greenish blue area. Interestingly, the uppermost portion of this greenish blue layer in the corrosion zone (d) also contains claringbullite (Cu_4Cl [$Cl_{0.29}(OH)_{0.71}$] ($OH)_6$) (Scott 2002), unambiguously identified on the basis of the very intense, characteristic OH-stretching bands observed at 3351 and 3436 cm^{-1} (Frost *et al.* 2003), mixed with $PbSO_4$. Beyond this layer, but still in the corrosion zone, a thin yellow-coloured layer (e) that was mostly abraded away during the polishing operation was observed to be particularly sensitive to irradiation with laser light. The spectrum, reproducibly recorded in several other similar yellow areas, is shown in Figure 8 (spectrum e) and was also observed by McCann *et al.* (1999) in the corroded δ phase of the $\alpha + \delta$ eutectoid of a corroded Chinese bronze money tree from the Eastern Han Period (AD 25–220). The spectrum of this layer resembles that of Cu_2O but lacks the band at 219 cm^{-1} (McCann *et al.* 1999). Finally, the outermost layer of corrosion (f) is dominated by a thick layer of Cu_2O.

Sulphur-containing corrosion products appear widespread in the subsurface layers of the patina. In particular, the detection of $PbSO_4$ dispersed throughout most of the corrosion layers seems to indicate that the artefact was exposed to a sulphur-rich environment, very likely anaerobic soils rich in bacterially produced H_2S: this would also justify the presence of black copper sulphides in the previously described interpenetration zone (a). When Gettens performed his analysis (Gettens 1951, 1969), he was unable to isolate enough of the black product originating from the corrosion of the eutectic and leaving dendrites of α bronze behind. His original XRD analysis of a fragment of material after removal of the outer corrosion product revealed Cu,
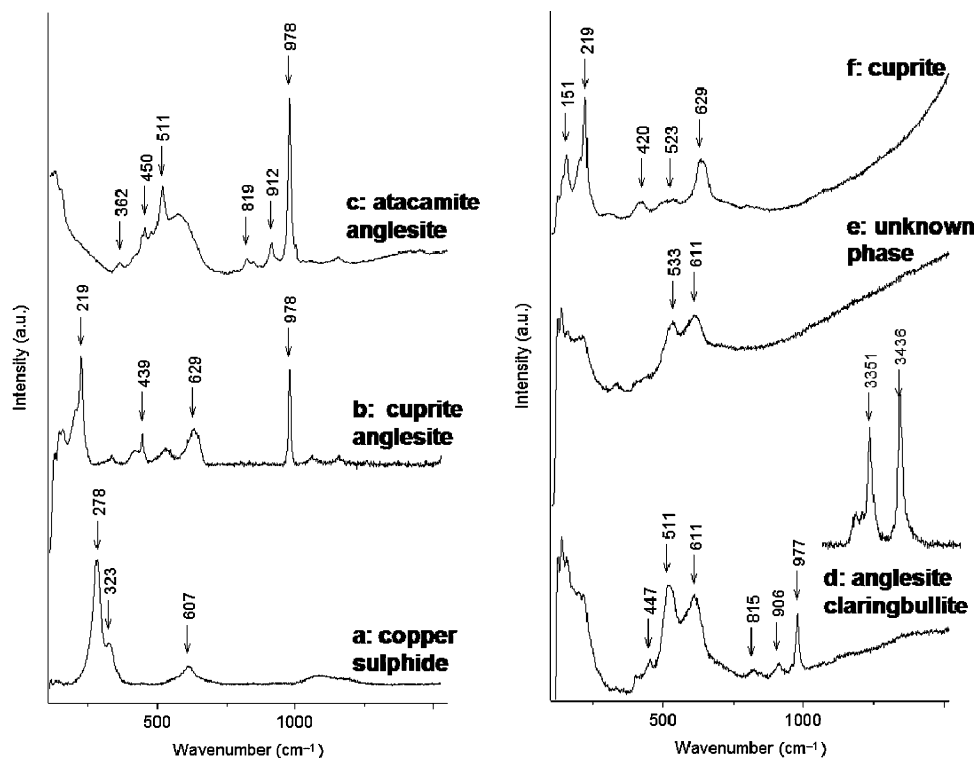
Figure 8 *Raman spectra of the various corrosion products from the outer wall of sample C for each region of interest (a–f) as shown below in Figure 9.*
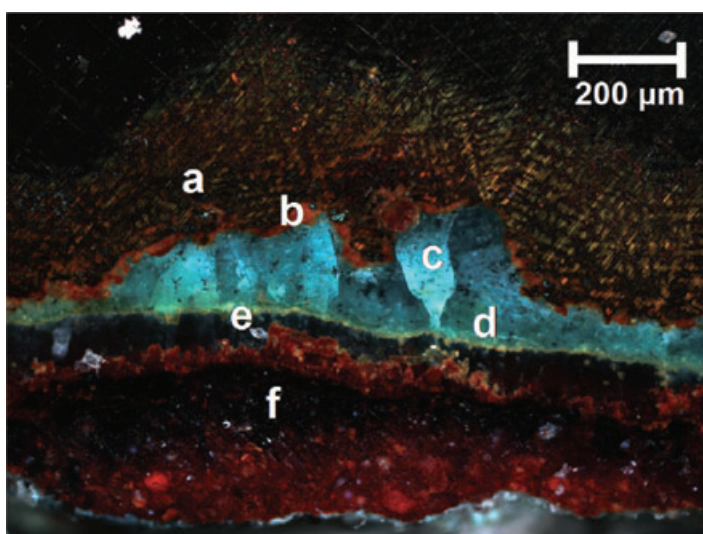

Figure 9 *An optical image of the outer wall of sample C with regions of interest (a–f). (See online for a colour version of this figure.)*
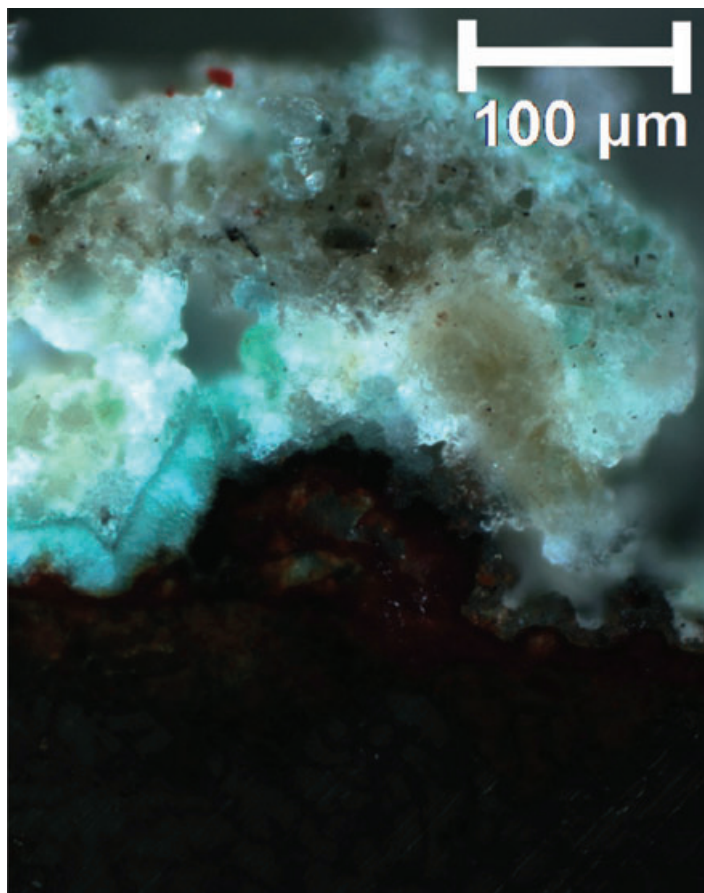
Figure 10 *An optical image of a cross-section showing the inner wall of sample C. (See online for a colour version of this figure.)*

a faint line for cassiterite (SnO_2) and one unidentified line. The present analysis, which can identify phases with improved resolution, allowed for identification of the dendritic black crystals as copper sulphide.

Inner wall of sample C The inner wall of sample C (and, consequently, of the vessel) shows different corrosion phenomena than what was described for the outer wall of the same sample (Fig. 10). As illustrated in Figure 11, the X-ray maps acquired with SEM/EDX show a well-preserved, clear outline of the surface of the original bronze, with Si-, Ca- and Cu-based corrosion products present in both the inner and outer corrosion layers. The detection of Si and Ca suggests that oxides from the environment are also embedded in the corrosion layer.

In the inner side of sample C, Raman microscopy identified malachite ($CuCO_3 \cdot Cu(OH)_2$) mixed with some calcite ($CaCO_3$) in the inner corrosion layer (b, Figs 11 and 12) and $CaCO_3$ and $PbSO_4$ in the uppermost, whitish portion of the patina (c, Figs 11 and 12). No Sn corrosion products were identified with either Raman or SEM/EDX. These results underscore that the mechanism and products of corrosions vary from place to place on the fragments and seem to
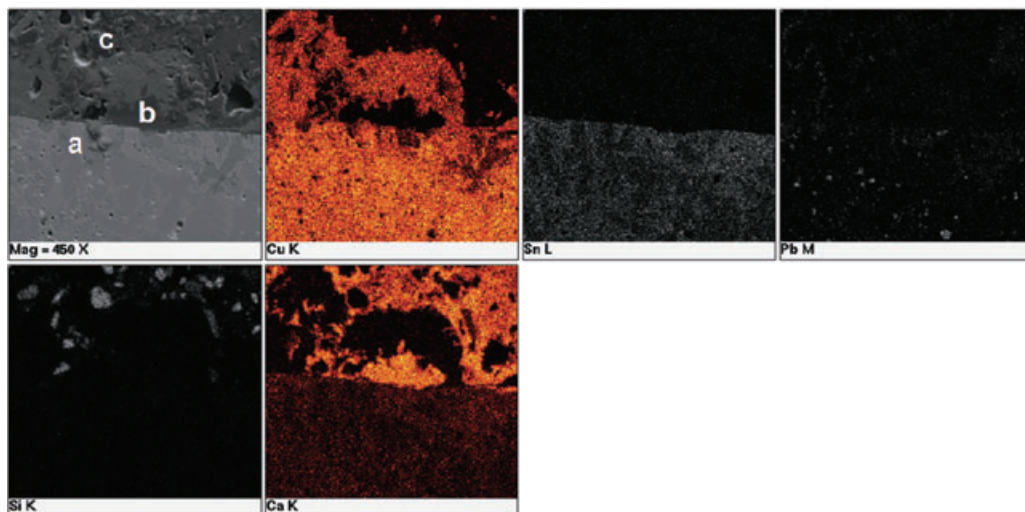
Figure 11   *SEM images and elemental distribution maps from the inner wall of sample C from the bronze fragment in Figure 10. (See online for a colour version of this figure.)*

suggest that in this particular spot the bi-layer of corrosion formed on the surface acts as a passivating, protective layer that inhibits further corrosion. Patinas such as the one observed here are said to be controlled by the cationic migration of Cu ions from the metallic bulk to the surface of the bronze and are typically characterized by the presence of $CuCO_3 \cdot Cu(OH)_2$ and absence of Cl-containing minerals (Robbiola *et al.* 1998).

Sample B   When compared to sample C, sample B exhibits a less complex patina structure. The cross-section highlights that the sample consists of a metallic core with a coarse dendritic structure consistent with casting, which is sandwiched between two corrosion layers with alternating Cu- and Sn-rich phases (Figs 13 and 14) with a high level of porosity. For the bulk region of this sample, the matrix is widely corroded, but the dendrites are mostly intact (Fig. 14 (b)). The dendritic structure is typical of Sn-rich bronzes, such as this one, known from Gettens' wet-chemical analysis to be composed of 72–74 wt% Cu, 20–22 wt% Sn and 4.1–4.6 wt% Pb (Gettens 1951, 1969). Raman spectra of the red corrosion layers identified the Cu-rich corrosion as Cu_2O, while SnO_2 and $PbSO_4$ were identified in the whitish, Sn-rich corrosion layers (Fig. 15). Although Sn is abundant in these layers, the Raman spectrum of SnO_2 is quite weak. A similar observation was also reported by McCann *et al.* (1999) and supports Gettens' suggestion that tin oxide may be in a near-amorphous state (Gettens 1951, 1969). Robbiola *et al.* (1998) also state that Sn-containing compounds in bronze corrosion layers are to be considered mainly as amorphous hydrated oxides, since these compounds are thermodynamically stable over a large range of pH and potentials.

In the centre of sample B, Pb globules are quite large and sometimes irregular in shape (Fig. 14 (b)), while in sample C, the Pb globules appear much smaller and with a regular spherical shape (Fig. 6 (b)). Some of the Pb globules in sample B surround small, pure Cu inclusions, a phenomenon that may be explained by either a solidification process at the time of casting or a corrosion process during burial (Chase 1979, 1994; Smith 1981; McCann *et al.* 1999).
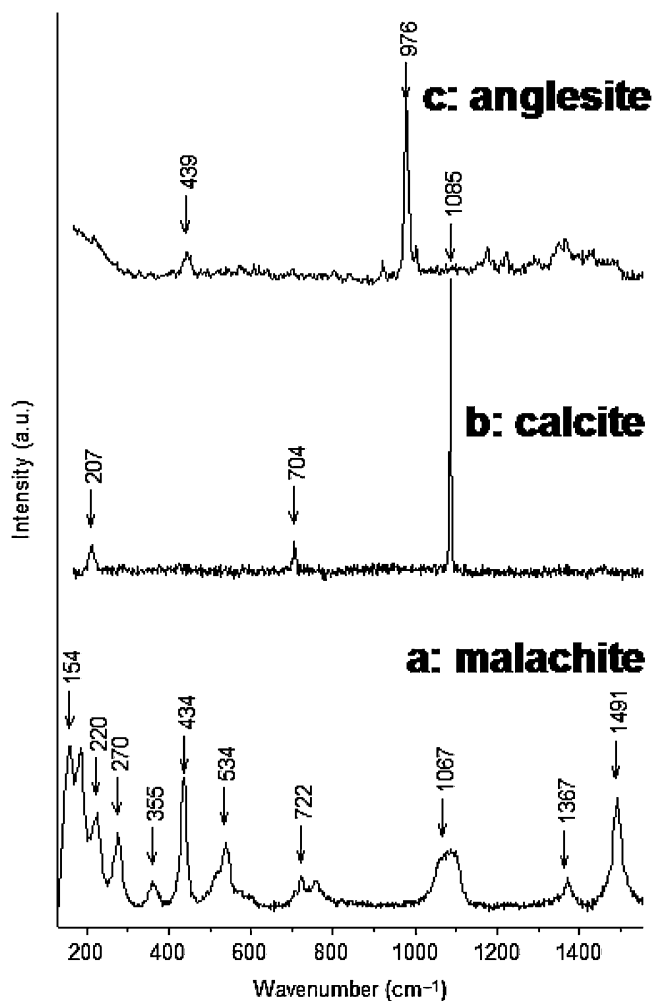
Figure 12   *Raman spectra of the various corrosion products from the inner wall of sample C in Figure 10.*

Comparison of modern analysis with historical scientific data   The description of the patina on the inner and outer walls of both fragments reported here highlights the fact that corrosion varies significantly even across a single vessel, with localized corrosion phenomena affecting different areas on the fragments. Overall, the corrosion products identified on the bronze fragments by the different techniques are listed in Table 1. A marked difference in corrosion products is observed not only between the inner and outer walls of the vessel, but also between the patina of the body of the vessel (sample C) and the patina at the foot (sample B). These observations underscore the occurrence of very localized corrosion processes, highly influenced by the micro-environment created in the burial soil and any other implements in direct contact with the object.

   Due to this variability in corrosion products, it is difficult to exactly correlate the phases described above with Gettens' original observations (Gettens 1951). In fact, Gettens described the presence of nantokite (CuCl) in contact with the corroding dendrites, followed by an
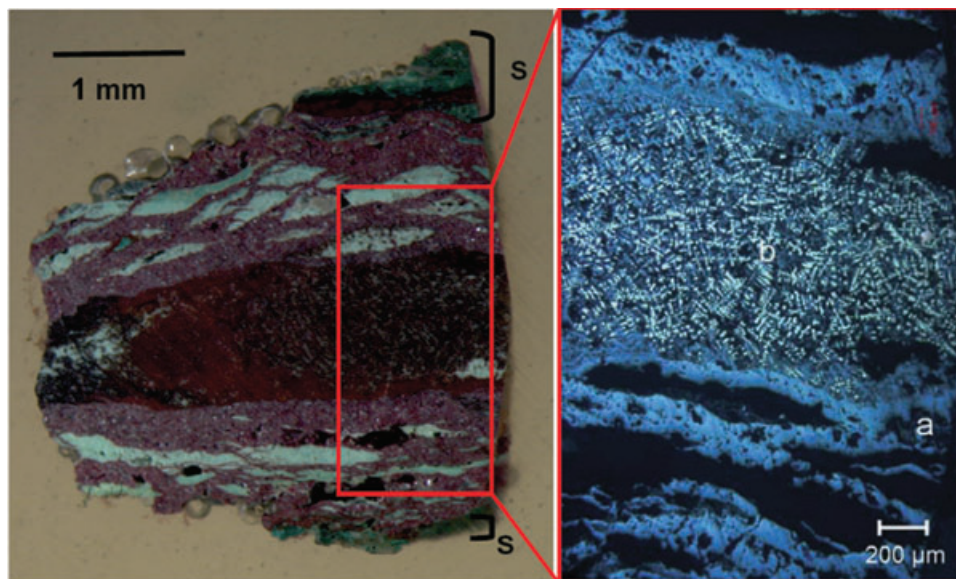
Figure 13   *Optical images of sample B, showing an etched dendritic core (etching occurred naturally during metallographic preparation) with two layered regions of corrosion products on the exposed surface of the vessel walls. (See online for a colour version of this figure.)*
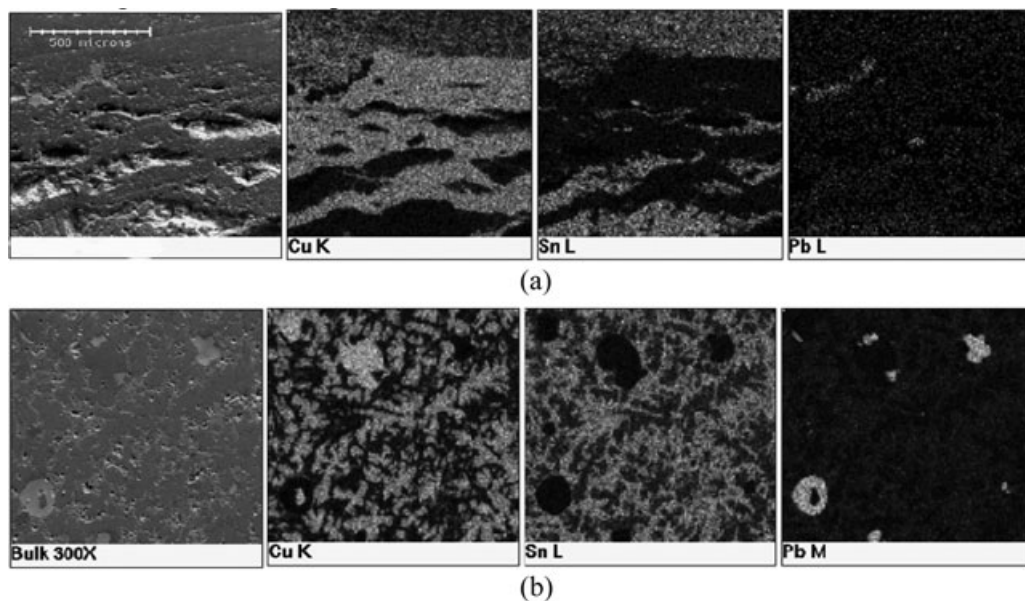

Figure 14   *SEM images and elemental distribution maps of sample B from the bronze fragment corresponding to (a) corrosion layers and (b) the bulk of the metal as labelled in the optical image in Figure 13.*
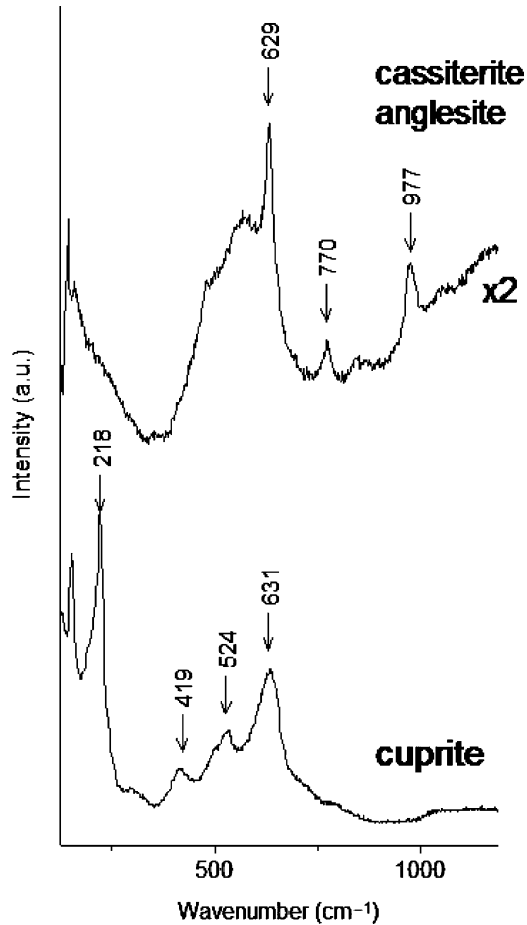
Figure 15   *Raman spectra of the various corrosion products from sample B in Figure 13.*

intermittent layer of redeposited metallic Cu, and, finally, a thick band of Cu_2O with white SnO_2 deposited in little disconnected seams throughout the Cu_2O, like 'streaks of fat' visible only at high magnification for one fragment. In other areas, the main corrosion product identified was $CuCO_3 \cdot Cu(OH)_2$, mixed with paratacamite ($Cu_2Cl\,(OH)_3$). Notwithstanding these differences, which are probably due to spatial variations of the corrosion phenomena, the most notable advancements made by using modern analytical techniques are the characterization of the corrosion products of Pb and the unambiguous identification of black copper sulphide corrosion products, which were impossible to isolate and hence identify with the tools available at the time of Gettens' studies (e.g., powder XRD) (Gettens 1951), due to their lower sensitivity on the micro-scale, and to the impossibility of performing spatially resolved analysis *in situ* on the cross-sections.

Identification of artificial patina on sample B   It is worth noting that Raman and FTIR microscopies also elucidated the composition of the outermost layers applied to disguise the joints in the original bronze fragments: a layer of superficial, applied stucco that is particularly

Table 1 *Description, elemental composition, molecular composition and overview of chemical phases identified for two samples (B and C) from a bronze fragment from an ancient Chinese vessel* (hu)

| Sample	Colour	Description	Elemental composition (SEM/EDX)	Molecular composition (Raman microscopy)	SR-XRD	Phases identified (overall)
C top	Shiny	Metallic core	Cu, Sn, Pb	N/A	Cu and $Cu_{41}Sn_{11}$, Pb	$-\alpha$ dendrites with $\alpha + \delta$ eutectic matrix and isolated Pb globules
C top	Black	Corrosion product around dendrites	Cu, Sn	Cu_2S	Cu_2O, SnO_2	Cu_2S
C top	Red	Corrosion on top of dendrite	Cu, Sn, Pb	Cu_2O, $PbSO_4$		Cu_2O, $PbSO_4$, SnO_2
C top	Light bluish green	Lower portion closer to metallic core	Cu, Sn, Pb	$CuCl_2 \cdot 3Cu(OH)_2$, $PbSO_4$		$CuCl_2 \cdot 3Cu(OH)_2$, $PbSO_4$, SnO_2
C top	Light bluish green	Upper portion closer to upper surface	Cu, Pb	$Cu_4Cl[Cl_{0.29}(OH)_{0.71}](OH)_6$, $PbSO_4$		$Cu_4Cl[Cl_{0.29}(OH)_{0.71}](OH)_6$, $PbSO_4$
C top	Yellow		Cu	Cu_2O species with altered Raman spectrum or different species		
C top	Bright red	Uppermost layer	Cu, Sn, Pb, Cl	Cu_2O		Cu_2O, SnO_2, SiO_2, $PbSO_4$, chlorinated copper compounds
C bottom	Light green	Corrosion layer closer to metallic core	Cu, some Ca	$CuCO_3 \cdot Cu(OH)_2$, traces of $CaCO_3$	N/A	$CuCO_3 \cdot Cu(OH)_2$, $CaCO_3$
C bottom	Greyish white	Intermediate corrosion layer	Ca, some Pb, Si	$CaCO_3$	N/A	$CaCO_3$, SiO_2, Pb corrosion products
C bottom	Light greyish green	Outermost corrosion layer	Ca, Pb, Si	$PbSO_4$	N/A	$PbSO_4$, SiO_2, $CaCO_3$
B	Reddish brown, ruby red or dark red	Alternating with whitish green corrosion	Cu, Pb	Cu_2O	N/A	Cu_2O, Pb corrosion products
B	Whitish green		Cu, Sn, Pb	SnO_2, $PbSO_4$	N/A	SnO_2, $PbSO_4$, or possibly Cu sulphate
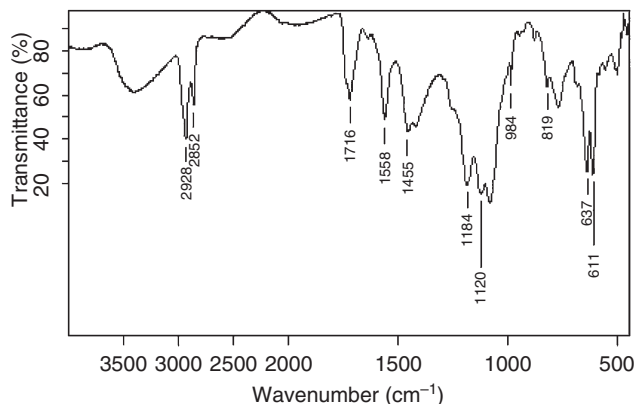
Figure 16   *A micro-Fourier transform infrared (FTIR) spectrum of a region of fake patina in sample B from the bronze fragment.*

evident in cross-section B (Fig. 13: bright green layer at very top and very bottom, marked 's'). As illustrated in Figure 16, the FTIR spectrum showed that the stucco is a mixture of barium sulphate ($BaSO_4$), emerald green (copper acetoarsenite-$Cu(C_2H_3O_2)_2 \cdot 3Cu(AsO_2)_2$), shellac and $CaCO_3$, while Raman microscopy confirmed emerald green as pigmenting material, mixed with ultramarine blue (Fig. 17). The new analysis confirmed and refined initial findings by Gettens (1969), who suspected the presence of shellac by a characteristic smell upon burning and by spectroscopic analysis after resin extraction, which detected large amounts of Zn and Cu, and lesser amounts of Si, Al, Ba (as barite, confirmed with XRD) and As (as emerald green, identified by microscopical examination). The identification of emerald green as pigmenting material ascribes the application to a date after 1800, when the pigment was discovered and successively commercially manufactured in Europe (Fiedler and Bayard 1997); however, it should be noted that emerald green pigment distribution and availability in China is unknown.

Synchrotron radiation X-ray diffraction

Although full account of the SR-XRD results has been given previously in Young *et al.* (2006), non-destructive SR-XRD results are summarized here and compared with the destructive examination carried out on the polished cross-section of sample C. The location where sample C was removed on the larger bronze fragment (Fig. 3 (a)) is the same as that where SR-XRD was performed.

In summary, SR-XRD patterns were collected every 20 μm step from the upper edge of the outer wall to 1.1 mm into the bulk of the fragment at an angle of 30° with respect to the sample surface. A gradual transition from surface corrosion products (Cu_2O and SnO_2) to the bulk metallic phases (Cu, $Cu_{41}Sn_{11}$ and Pb) is observed. The depth of corrosion varies depending on where the sample is positioned; in this case, the corrosion layer is about 370 μm deep, as indicated by phase disappearances/emergences, suggesting that the corrosion layer is relatively thin and that the bulk of the fragment is uncorroded. These conclusions are confirmed by the metallographic cross-section shown in Figure 5. Diffraction patterns indicate that the corrosion products have a fine, untextured grain structure and the bulk metal has a coarse, untextured grain structure, the latter indicating that the vessel was produced by casting instead of cold- or hot-working where a fine, textured grain structure would be observed for the bulk metal.
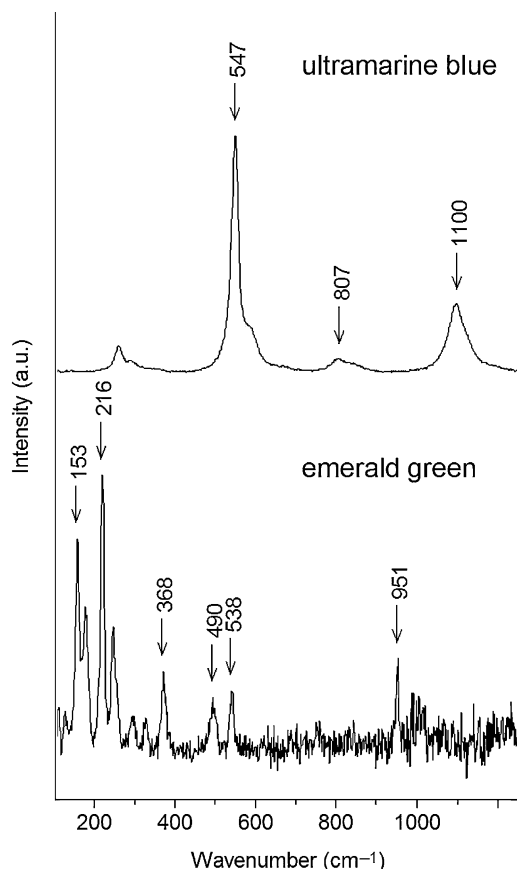
Figure 17 *A Raman spectrum of blue and green particles in the fake patina of sample B from the bronze fragment.*

From this earlier study (Young *et al.* 2006), three distinct advantages of using SR-XRD are that: (a) both the bulk and corrosion layers of the sample are analysed non-destructively and their approximate thicknesses can be measured; (b) the major phases present are identifiable; and (c) the original fabrication technique can be determined. The potential of SR-XRD to elucidate bronze corrosion products non-destructively has already been extensively described (De Ryck *et al.* 2003; Pantos *et al.* 2005; Salvado *et al.* 2005). Furthermore, in addition to SR-XRD, other SR techniques such as XRF, XAS, FTIR and radiography can also be used alone or in combination to non-destructively study ancient metal artefacts (Harbottle *et al.* 1986; Janssens *et al.* 2000; Stephenson *et al.* 2001; Araujo *et al.* 2003; De Ryck *et al.* 2003; Schreiner *et al.* 2003; Grolimund *et al.* 2004; Newbury *et al.* 2004, 2006; Pantos *et al.* 2005).

Inductively coupled plasma optical emission spectroscopy (ICP–OES)

ICP–OES on the bulk region of the cross-section of sample C revealed a composition of 77.03 wt% Cu, 18.17 wt% Sn, 4.44 Pb, 0.03 Zn, 0.02 Fe, <0.01 Ni, 0.10 As, <0.01% Cr and <0.01% Sb, which refines the composition observed by Gettens, where the bulk metal was found

to consist of 72–74 wt% Cu, 20–22 wt% Sn, 4.1–4.6 wt% Pb and 0.1–1.0 wt% As (Gettens 1951, 1969). Using the more accurate ICP–OES technique, it is also possible to detect trace elements not detected earlier by Gettens, such as Zn, Fe, Ni, Cr and Sb, which can be important in the authentification and origin of ancient objects (Niederschlag *et al.* 2003; Pollard and Heron 2008).

Secondary ion mass spectrometry (SIMS)

During SIMS analysis, a beam of Ga ions is sputtered on to the surface of a sample, in this case, an uncorroded region in the cross-section of sample C. The sputtered elements are ionized and analysed by time-of-flight spectroscopy, in a manner similar to mass spectroscopy (MS). Unlike MS, which consumes a whole sample and thus provides average values for all ions, SIMS provides a measurement on a very small local area (~100×100 μm^2) and therefore is nearly non-destructive, only requiring a very small amount of sample (<1 mm^3). Similar low sample quantities are used in thermal ion mass spectrometry (TIMS), where a small amount of sample is dissolved in acid, the Pb is separated electrochemically on to an electrode, the electrode with the deposited Pb is heated in a mass spectrograph and the intensities of the Pb isotopes are measured. SIMS and TIMS have both been used extensively for geological studies of Pb-containing artefacts (Gale and Stos-Gale 1982; Pernicka *et al.* 1990; Stos-Gale *et al.*, 1997; Weeks, 1999; Spoto 2000) and more specifically on Chinese artefacts (Mabuchi *et al.* 1985; Barnes *et al.* 1987; Mabuchi and Hirao 1987; Chase *et al.* 1990; Hargrove 1997; Yeung *et al.* 2000).

SIMS has several advantages over other analytical methods. Unlike ICP–OES, SIMS can provide the full spectrum of elements present with very high sensitivity (Benninghoven *et al.* 1987) as well as information about the isotopes present. Specifically, Pb isotopes are of interest in the study of ancient bronzes. Pb isotopes are the stable result of the natural decay of radioactive elements (e.g., ^{238}U decays to ^{206}Pb, ^{235}U decays to ^{207}Pb and ^{232}Th decays to ^{208}Pb) (Rosman and Taylor 1998), providing insight into the geological history of the ore and its mode of formation (Faure 1977). The range of the Pb-isotopic compositions varies significantly depending upon the mining site, as shown specifically for Chinese mining sites (Ikonnikov 1975; Mabuchi and Hirao 1987; Jin 1991; Jin *et al.* 1998b,c). Peng *et al.* (2000) examined the geographical origin of Pb isotopes in China and divided the Chinese ore sources into three areas by Pb isotope ratios; high radiogenic lead (^{208}Pb/^{206}Pb less than 2), middle ratios (^{208}Pb/^{206}Pb from 2 to 2.16), and north-eastern sources (^{208}Pb/^{206}Pb greater than 2.16). High-radiogenic lead, which is relevant to our discussion below, probably originated from polymetallic ore deposits formed from uranium in southwestern China.

Here, SIMS was performed on the bulk region of the cross-section of sample C. As shown in Figure 18, a surface map of total ion counts and elemental maps of ion counts for selected elements (Cu and Pb) was collected in scanning mode and shows similar microstructure to that observed in the SEM image of the bulk region of sample C (Fig. 6 (a)), with small Pb inclusions ~5–10 μm in size. In this particular image (Fig. 18), a larger than average Pb particle (~20 μm) was examined to achieve higher Pb count rates. In addition to the major (Cu) and minor elements (Sn, Pb) present in the bulk of the bronze fragment, trace elements (Ag, As, Ge, K, Na, Se, Si, Sr and Zn) were also observed and most probably originate as impurities within the metal ore used for casting. However, the source of Ge, Se and Sr is unclear: these elements may be artefacts from the chamber.

By analysing a highly polished surface, the individual spectral peaks corresponding to the four main Pb isotopes (^{204}Pb, ^{206}Pb, ^{207}Pb and ^{208}Pb) are well separated from each other, thus indicating excellent mass resolution, as shown in Figure 19.
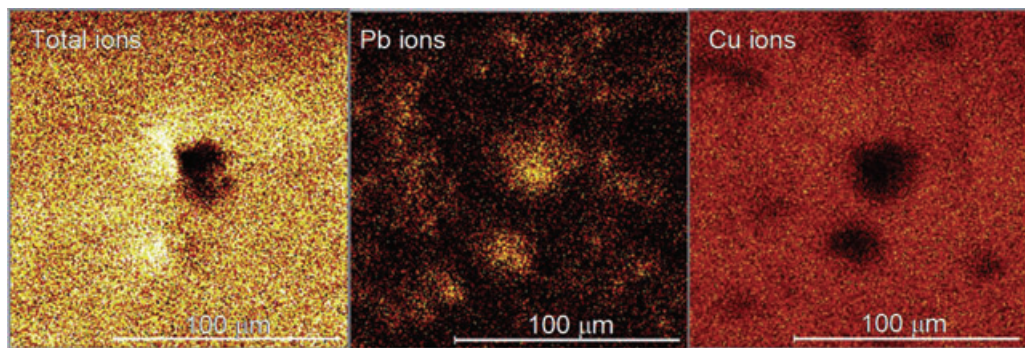
Figure 18   *SIMS images for the total ion count and for selected elements (Cu, Sn, Pb, Fe, Si and Zn) collected in scanning mode, showing a couple of Pb globules in a Cu-rich matrix from the bulk metal of sample C. (See online for a colour version of this figure.)*
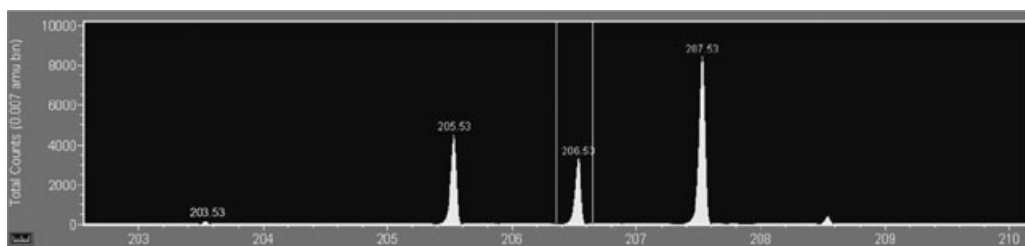

Figure 19   *A typical SIMS spectrum taken from a Pb globule, showing the four main isotopes (^{204}Pb, ^{206}Pb, ^{207}Pb and ^{208}Pb) and a spurious peak (^{209}Pb). The two white lines surrounding the peak at 207 illustrate the measuring width (~0.3) for each measured region.*

Table 2 presents the ^{204}Pb/^{206}Pb, ^{207}Pb/^{206}Pb and ^{208}Pb/^{206}Pb isotope ratios for six areas of the NIST Pb standard (SRM 981) and five areas of sample C. Averages for these areas are also given, together with the standard deviation, and are within error of the values found when conducting a weighted average based on the ion numbers (the weighted averages are thus not given in Table 2). The NIST measurements (the first three performed immediately before and the last three after the measurements on sample C) provide isotope ratios very close to the theoretical NIST values, showing that the instrument is well calibrated and not drifting during the bronze measurement. The small difference between measured and theoretical NIST ratio was used as a calibration factor to correct the measured ratio for the bronze fragment. Its isotopic ratios listed in Table 2 thus incorporate three types of corrections: background subtraction, spillage correction (described in the previous paragraph) and NIST calibration correction. After correction, the ^{208}Pb/^{206}Pb isotope ratio of 1.8933 for the 'Kelley' bronze falls clearly in the area of high-radiogenic lead.

Also listed in Table 2 are ranges of isotopic ratios for several other ancient Chinese artefacts from the St Louis Art Museum (11 artefacts: Hargrove 1997), from the Arthur M. Sackler Collections (222 artefacts: Barnes *et al.* 1987; Chase *et al.* 1990) and from two controlled excavations in China (seven artefacts: Yeung *et al.* 2000; Z. Jin, pers. comm.). The results from Yeung *et al.* (2000) show Pb isotope values determined by both SIMS and TIMS on the same samples, with good experimental agreement. The ranges of the Pb isotopic ratios for 11 ancient

Table 2 *Pb-isotope ratios from SIMS measurements and from the literature (Barnes* et al. *1987; Chase* et al. *1990; Hargrove 1997; Yeung* et al. *2000) or personal communication from Dr Jin (Jin)*

Run no.	Area	Measurements	Total no. of Pb counts	$^{204}Pb/^{206}Pb$	$^{207}Pb/^{206}Pb$	$^{208}Pb/^{206}Pb$
1	1	Pb standard (SRM 981)	177 769	0.05940	0.9113	2.1408
2	2		156 352	0.05870	0.9009	2.1217
3	3		110 977	0.05881	0.9115	2.1523
6	4		133 929	0.06074	0.9188	2.1477
10	5		148 504	0.05955	0.9030	2.1262
11	6		109 217	0.05603	0.9177	2.1666
	1–6	Sum 1–6*	836 748	**0.0590**	**0.9099**	**2.1406**
		St. dev. of sum 1–6†		0.0016	0.0074	0.0168
		Pb standard (SRM 981)§		0.0590	0.9147	2.168
		Theoretical NIST value				
4	1	'Kelley' bronze fragment	141 534	0.0443	0.7152	1.8695
5	2		65 368	0.0479	0.7237	1.8725
7	3		149 572	0.0441	0.7075	1.8410
8	4		166 211	0.0458	0.7117	1.8524
9	5		126 659	0.0454	0.7118	1.8509
	1–5	Sum 1–5¶	649 344	**0.0456**	**0.7218**	**1.8933**
		St. dev. of sum 1–5†		0.0015	0.0061	0.0134

Literature values	$^{204}Pb/^{206}Pb$	$^{207}Pb/^{206}Pb$	$^{208}Pb/^{206}Pb$
St Louis Art Museum (11 artefacts) (Hargrove 1997)	0.046–0.058	0.74–0.90	1.94–2.20
Sackler Museum (97 artefacts—Shang Period) (Barnes *et al.* 1987)	0.041–0.059	0.68–0.90	1.87–2.24
Sackler Museum (three *hu* vessels—Shang Period) (Barnes *et al.* 1987)	0.044–0.055	0.72–0.86	1.93–2.12
Sackler Museum (125 artefacts—Western Zhou Period) (Chase *et al.* 1990)	0.045–0.059	0.72–0.91	1.91–2.20
Sackler Museum (two *hu* vessels—Western Zhou Period) (Chase *et al.* 1990)	0.049–0.055	0.78–0.85	2.01–2.10
Sackler Museum (*hu* vessel, cat. #60) (Barnes *et al.* 1987)	**0.04412**	**0.7181**	**1.9268**
Sackler Museum (*hu* vessel, cat. #58) (Barnes *et al.* 1987)	0.04808	0.7867	1.9905
pan basin (no. zy334, SIMS) (Yeung *et al.* 2000)	**0.0441**	**0.7109**	**1.876**
zun vase (no. zy332, SIMS) (Yeung *et al.* 2000)	**0.0444**	**0.703**	**1.869**
Fu Hao tomb ZY-093 *fang yi* M5: 791 (Jin)	**0.04389**	**0.7175**	**1.8953**
Fu Hao tomb ZY-142 *zun* M5: 320 (Jin)	**0.04541**	**0.7287**	**1.9161**
Fu Hao tomb ZY-139 Steamer M5: 865 (Jin)	**0.04261**	**0.6993**	**1.9272**
Fu Hao tomb ZY-138 *hu* M5: 795 (Jin)	**0.04540**	**0.7326**	**1.9443**
Fu Hao tomb ZY-141 *jia* M5: 751 (Jin)	0.05532	0.8626	2.1237

*Ion counts were added for all six measurements for each isotope.

†Standard deviations of ratios.

§Standard reference lead (SRM 981) from NIST.

¶Counts were added for all five measurements for each isotope.

Chinese bronzes from the St Louis Art Museum collection were measured by TIMS at NIST and reported by Hargrove (1997). These ratios are all higher than those measured here on the fragment and only one (a *Gu*, St Louis acc. no. 217.1950) of the vessels falls into the high-radiogenic Pb area.

Ranges for Pb-isotopic ratios from 132 TIMS measurements for 125 ancient Chinese bronzes from the Western Zhou Period (Chase *et al.* 1990) and 123 TIMS measurements for 97 ancient

Chinese bronzes from the Shang Period (Barnes *et al.* 1987) in the Sackler Collections are also listed in Table 2. Assessing values for the $^{208}Pb/^{206}Pb$ isotope ratio below a value of 2.0, a third (65/97) of the Shang bronzes contain high-radiogenic lead. Furthermore, only five of the 125 Western Zhou bronzes (Chase *et al.* 1990) and one of the 85 Eastern Zhou bronzes (Chase *et al.* 1995) in the Sackler Collections have a value below 2.0 for the $^{208}Pb/^{206}Pb$ ratio. Although not shown in Table 2 and beyond the scope of this study, it should be mentioned that 86 measurements from 82 ancient Chinese bronzes from the Eastern Zhou Period were also determined by Chase *et al.* (1995). The one Eastern Zhou bronze with high-radiogenic lead, a *he*-cup (no. 86) with inlay, is anomalous; interestingly, the inlay appears to have been applied in modern times. Like $^{208}Pb/^{206}Pb$ isotope ratios, similar trends are also observed in the $^{207}Pb/^{206}Pb$ and $^{204}Pb/^{206}Pb$ isotope ratios.

Two of the 125 ancient Chinese bronzes from the Western Zhou Period are *hu* vessels similar to the *hu* fragment examined here. Their Pb-isotopic ratios are in the middle of the range and neither is close to the ratio ranges observed for the present fragment. Their compositions (88.3 wt% Cu, 9.9 wt% Sn, and 0.64 wt% Pb and 74.6 wt% Cu, 2.7 wt% Sn and 19.1 wt% Pb, respectively) are also significantly different from the present fragment (72–74 wt% Cu, 20–22 wt% Sn and 4.1–4.6 wt% Pb: Gettens 1951, 1969) and based on their Pb-isotopic ratios they probably do not have the same provenance as the *hu* fragment here.

Three of the 97 ancient Chinese bronzes from the Shang Period are *hu* vessels similar to the fragment examined here. As listed in Table 2, two of the *hu* vessels contain high-radiogenic lead. Although its composition (66.0 wt% Cu, 5.8 wt% Sn and 29.1 wt%Pb) is significantly different than the present fragment (72–74 wt% Cu, 20–22 wt% Sn and 4.1–4.6 wt% Pb: Gettens 1951, 1969), the first *hu* vessel (ring foot of *hu* vessel catalogue no. 60, Table 2) has isotopic ratios very close to those measured on the present fragment. The second *hu* vessel (ring foot of *hu* vessel no. 58, Table 2) is just at the cut-off point for high–radiogenic lead, but its composition (78.3 wt% Cu, 21.9 wt% Sn and 2.69 wt% Pb) is much closer to the present *hu* fragment. The second *hu* vessel and the 'Kelley' bronze vessel both have the decoration feature of three 'bowstrings' as the top décor register, and both employ the same squared double spiral with protruding elements; this double spiral occurs on the foot of the 'Kelley' bronze vessel and just below the three bowstrings at the top of the Sackler *hu* vessel. Bagley (1987) dates the Sackler *hu* vessel to the 13th century BC and relates it to the typologically more advanced oval-bodied *hu* in Fu Hao's tomb, one of which (*hu* M5: 795) appears in Table 2.

Using the multivariate statistical methods pioneered by Edward V. Sayre *et al.* (Barnes *et al.* 1988), the lead isotope ratios and compositions of the Sackler bronzes have been grouped. A diagram of the chronological distributions of these groups has been created by Chase (1996). A revised version of this diagram, which highlights the high-radiogenic lead groups with black bars, is shown in Figure 20. Groups 7, 8, D and E lie in the high-radiogenic lead area. Group 8 contains bronzes from the middle Shang and early Anyang Periods. Group 7 contains bronzes from all Anyang Periods, as well as a small number (five) of Western Zhou bronzes. High-radiogenic leads are almost exclusively from the Shang Period.

Dr Jin of the University of Science and Technology of China has determined the isotope ratios in over 500 excavated bronzes from China, covering all periods of Chinese history (Jin *et al.* 1994, 1995; Jin 2000; Hirao 2001). Many of the analyses of early bronzes are published (Jin *et al.* 1994, 1995; Jin 2000; Hirao 2001), but the Shang Period material has not yet received full publication. The picture that emerges is complex. The earliest pre-Anyang bronzes are not made
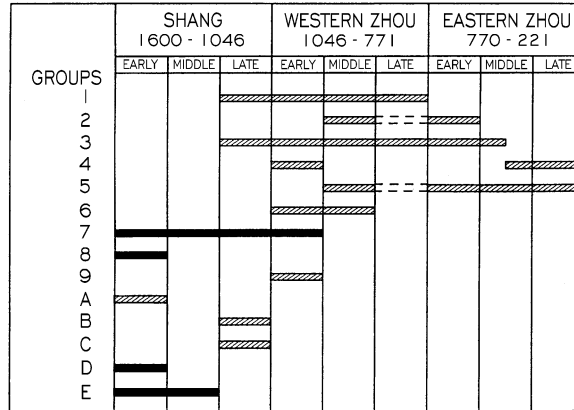
Figure 20   *A diagram of the chronological distributions of lead isotope groups from a large number of bronzes in the Sackler Museum. The black bars highlight the high-radiogenic lead groups.*

with high-radiogenic leads, but rather from leads in the middle range and, in the case of Erlitou, leads in the northeastern range, above 2.16 for ^{208}Pb/^{206}Pb. The enigmatic bronzes from Sanxingdui in Szechuan are made with extremely radiogenic leads. These leads, or similar leads, continue on into the Shang Period and are encountered in the bronzes from Xingan Dayangzhou. The bronzes from Erligang and Panlongcheng include both high-radiogenic lead and lead in the middle range. As the Anyang Period progresses, lead isotope ratios spread from the high-radiogenic area to the non-radiogenic part of the diagram. In subsequent periods (Eastern Zhou, Western Zhou and Han), most of the leads determined by Dr Jin fall into the middle or northeastern part of the diagram.

Based on these results, the Shang Period bronze casters had access to different lead sources at different times. During the early Anyang Period, sources of high-radiogenic lead were being used. In the statistical groups from the Sackler bronzes, two large groups (groups 7 and 8) fall into this high-radiogenic area. These groups correspond closely with lead isotope ratios from many bronzes in the Shang Periods II and III analysed by Dr Jin (the periodization of the bronzes analysed in that study was assigned from archaeological evidence). However, some of the bronzes from this period have lead isotope ratios from a less radiogenic lead source, possibly the same source used to make the Erlitou Period bronzes. During the later Anyang Period, bronzes in the non-radiogenic end of the distribution tend to fall on a different growth line than that used at the Erlitou Period.

Two bronzes from Sanxingdui, analysed by Yeung *et al.* (2000), are shown in Table 2. Their comparative study, using both SIMS and TIMS for lead isotope analysis of four ancient Chinese metallic artefacts, showed that SIMS was slightly less accurate, but still very useful to differentiate high-radiogenic leads in some ancient bronzes from other leads. In particular, they examined a *pan* basin made from leaded bronze (sample no. zy334, Shang Period, excavated at Sanxingdui in the Szechuan Province), consisting of 67.5% Cu, 10.9% Sn and 20.3% Pb. Their Pb isotope ratios by SIMS (Table 2) are, within experimental error, the same as our results for the present bronze fragment. This is also true for an unalloyed copper *zun* vase (no. zy332, Shang Period: 93.1% Cu, 1.4% Sn and 0.2% Pb). However, the Pb-isotope ratios for the other two less ancient artefacts, a hair pin (Western Zhou, 1100–771 BC) made from unalloyed tin and an artefact (Warring States, 475–221 BC) made from unalloyed lead, do not match our fragment and are
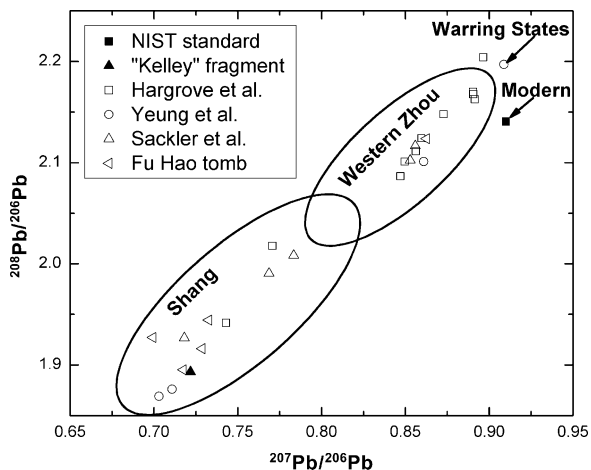
Figure 21   *Pb-isotopic data for ancient Chinese bronzes. The ellipses are shown to highlight the ranges where most bronzes from the Shang and Western Zhou Periods are found.*

much closer to the ratios of artefacts from the Western Zhou Period, as reported in the Sackler study (Chase *et al.* 1990). Considering the lead isotope trends discussed above, Yeung *et al.* (2000) noted that a high-radiogenic Pb ratio content is found for most Shang bronzes, which is different from the value for ordinary (non-radiogenic) lead in China or the NIST standard. Our fragment is in the low range, with a value 0.722 ± 0.006, and thus closer to the values found for the two Shang Period artefacts studied by Yeung *et al.* (2000).

Five bronzes from the Fu Hao tomb, 'the most remarkable single find ever made at the Anyang site' (Bagley 1980), are also shown in Table 2. Dr Jin determined the Pb-isotope ratios of 14 bronzes from the Fu Hao tomb. Eight of these are high-radiogenic leads, and the lead-isotope ratios of the huge double *fang yi* (M5: 791) correspond almost exactly to those from our 'Kelley' bronze fragment.

By plotting the ratios of $^{208}Pb/^{206}Pb$ against $^{207}Pb/^{206}Pb$, as shown in Figure 21, it can be shown that bronzes from the Shang Period tend to cluster in the bottom left region of the graph (high-radiogenic lead), while the bronzes from the Western Zhou Period tend to cluster in the middle region, and bronzes from the Warring States and Modern Periods tend to cluster in the upper right. Our bronze fragment falls on the low end of the Shang Period cluster, which corroborates the hypothesis that it originated from metal from the Shang Period, and very possibly from an Anyang foundry active in Anyang Period II or III.

It is worth noting that the Fu Hao bronzes cover a fairly wide range, and seem to be quite evenly spaced; the range is much wider and more even than many of the early tombs from Anyang represented in Dr Jin's data. This result implies that the use of multiple ore sources and/or an active metals trade was occurring during this period. It should be noted here that a huge amount of bronze was found at the Fu Hao tomb, with a combined weight of over 1.6 metric tons (Buckley-Ebrey 2007). While the reuse of old metal as scrap will give lead-isotope ratios from sources that may not be contemporary with a casting, the fact that high-radiogenic lead is rare in the Western Zhou Period and almost non-existent in the Warring States Period suggests that scrap may not have played an important role in Chinese ceremonial vessel production.

CONCLUSIONS

Using modern analytical techniques, it is possible to deepen our understanding of the creation and subsequent corrosion of artefacts such as the 'Kelley' bronze fragments from a *hu* vessel originally attributed to the Zhou Period. The re-examination of the 'Kelley' bronze fragments 50 years after their first investigation allowed for the combination and comparison of traditional and more advanced analytical techniques, to arrive at a detailed morphological, metallurgical, chemical and elemental characterization of the bulk metal and associated corrosion products with good spatial resolution.

ICP–OES provides elemental information about the bulk material, with much higher accuracy than traditional methods previously performed by Gettens. Here, the alloy composition of the fragments was determined to be 77.03 wt% Cu, 18.17 wt% Sn, 4.44 wt% Pb and 0.03 wt% Zn and other minor elements using ICP–OES.

A combination of SEM/EDX, which allows for the effective visualization of the elements present within the core and in the interior and exterior corrosion layers, and Raman microspectroscopy, which allows for the determination of major and minor corrosion phases with high spatial resolution, on cross-sectioned samples allowed for complete molecular characterization and highly spatially resolved mapping of corrosion phases. Specifically, different corrosion products were highlighted: cuprite, copper sulphides, carbonates (malachite), chlorides (atacamite and claringbullite), tin oxides (cassiterite), lead sulphates and extraneous compounds derived from the burial soil such as calcium carbonates and silicates. Furthermore, a fake patina of barium sulphate, emerald green, ultramarine and shellac was also identified, which had been applied to camouflage the seams between original parts of the vessel and modern additions.

Microstructural data obtained with invasive means of analysis on sectioned samples were also compared with non-invasive SR-XRD measurements on the intact fragments and indicate that SR-XRD can accurately measure the thickness of the corrosion layer and also identify major phases in the corrosion layers (e.g., Cu_2O and SnO_2) and the bulk metal (e.g., Cu, $Cu_{41}Sn_{11}$ and Pb), thus demonstrating great potential as an accurate, non-destructive technique for the characterization of ancient bronzes.

As determined by SIMS, the Pb-isotope ratios from the bronze fragment overlap with other extensive literature measurements on Shang Period bronzes. Therefore, the present SIMS analysis supports the re-attribution of the 'Kelley' bronze fragments to the Shang Period. Furthermore, the Pb-isotope analysis provides clues to the origin of the ore used for the bronze object and enables speculation on the time period of manufacture.

In conclusion, complete characterization of ancient Chinese bronzes and, in this study, the 'Kelley' bronze fragments is achieved only with a combination of complementary techniques. In the future, spatially resolved SR-XRD has great potential for *in-situ*, non-invasive characterization of both corrosion layers and metallic core. As synchrotron facilities become more advanced and available, combined SR techniques (e.g., SR-XRD and SR-XRF) will allow *in-situ* non-destructive and spatially resolved studies of ancient artefacts, thus reducing or even eliminating the need to destructively sample ancient precious objects, which are important surviving testimonies of the societies that produced them.

REFERENCES

Araujo, M. F., Pinheiro, T., Valerio, P., Barreiros, A., Simionovici, A., Bohic, S., and Melo, A., 2003, Analysis of a Roman cenfaurus from Canas de Senhorim (Portugal)—comparative study using EDXRF and SXRF, *Journal de Physique IV*, **104**, 523–6.

Bagley, R. W., 1980, *The High Yinxu Phase (Anyang Period): the great Bronze Age of China*, 177–213, The Metropolitan Museum of Art/Alfred A. Knopf, New York.

Bagley, R. W., 1987, *Shang ritual bronzes in the Arthur M. Sackler Collections*, vol. 1, Harvard University Press, Cambridge, MA.

Bagley, R. W., 2001, *Ancient Sichuan: treasures from a lost civilization*, Princeton University Press, Princeton, NJ.

Barnes, I. L., Chase, W. T., and Deal, E. C., 1987, Appendix 2: lead isotope ratios, in *Shang ritual bronzes in the Arthur M. Sackler Collections* (R. W. Bagley), Ancient Chinese Bronzes from the Arthur M. Sackler Collections, vol. 1, Harvard University Press, Cambridge, MA.

Barnes, I. L., Chase, W. T., Holmes, L. L., Joel, E. C., Meyers, J. P., and Sayre, E. V., 1988, The technical examination, lead isotope determination, and elemental analysis of some Shang and Zhou Dynasty bronze vessels, in *Second International Conference on the Beginning of the Use of Metals and Alloys, Zhengzhou, China, 21–26 October 1986*.

Benninghoven, A., Rudenaure, F. G., and Werner, H. W., 1987, *Secondary ion mass spectrometry: basic concepts, instrumental aspects, applications and trends*, New York, Wiley.

Buckley-Ebrey, P., 2007, Bronzes from Fu Hao's tomb, in *A visual sourcebook of Chinese civilization*, University of Washington; available at http://depts.washington.edu/chinaciv/archae/2fuhbron.htm (accessed 22 January 2010).

Chase, W. T., 1979, Solid samples from metallic antiquities and their examination, in *Cultural property and analytical chemistry, International Symposium on the Conservation and Restoration of Cultural Property*, 73–109, Tokyo National Research Institute of Cultural Properties [and] Organizing Committee of International Symposium on the Conservation and Restoration of Cultural Property, Tokyo.

Chase, W. T., 1994, Chinese bronzes: casting, finishing, patination and corrosion, in *Ancient and historic metals; conservation and technology*, (eds. D. Scott, J. Podany and B. B. Consaidine), 63–74, 85–117, Getty Conservation Institute, Marina del Rey, CA.

Chase, W. T., 1996, lead isotope ratio analysis of Chinese bronzes: examples from the Freer Gallery of Art and Arthur M. Sackler Collections, in *The ancient Chinese and Southeast Asian bronze cultures: the proceedings of a conference held at the Edith and Joy London Foundation Property, Kioloa, NSW, 8–12 February 1988*, SMC Publishing, Taipei.

Chase, W. T., Barnes, I. L., and Joel, E. C., 1990, Appendix 6: lead isotope ratios, in *Western Zhou ritual bronzes from the Arthur M. Sackler Collections* (J. Rawson), Ancient Chinese Bronzes from the Arthur M. Sackler Collections, vol. 2A, Harvard University Press, Cambridge, MA.

Chase, W. T., Barnes, I. L., and Joel, E. C., 1995, Appendix 4: lead isotope ratios, in *Eastern Zhou ritual bronzes from the Arthur M. Sackler Collections* (J. F. So), Ancient Chinese Bronzes from the Arthur M. Sackler Collections, vol. 3, Harry N. Abrams, New York.

Chase, W. T., Notis, M. R., and Pelton, A. D., 2007, New Eh–pH diagrams of the copper–tin system, in *METAL07, ICOM-CC Metal Working Group triennial conference, Amsterdam (The Netherlands), 17–21 September 2007*.

De Ryck, A., Adriaens, A., Pantos, E., and Adams, F., 2003, A comparison of microbeam techniques for the analysis of corroded ancient bronze objects, *The Analyst*, **128**, 1104–9.

Eichhorn, P., 1988, Cuprit auf Bronze—ein Echtheitsbeweis?, *Arbeitsblaetter für Restauratoren*, Gruppe 2 (Heft 2), 235–9.

Faure, G., 1977, *Principles of isotope geology*, New York, Wiley.

Fiedler, I., and Bayard, M. A., 1997, Emerald green and Scheele's green, in *Artists' pigments: a handbook of their history and characteristics*, vol. 3 (ed. E. W. Fitzhugh), 226–7, National Gallery of Art/Oxford University Press, Washington, DC.

Frost, R. L., Williams, P. A., Kloprogge, J. T., and Martens, W., 2003, Raman spectroscopy of the copper chloride minerals nantokite, eriochalcite and claringbullilte—implications for copper corrosion, *Neues Jahrbuch für Mineralogie, Monatshefte*, **10**(1), 433–45.

Gale, N. H., and Stos-Gale, Z. A., 1982, Bronze Age copper sources in the Mediterranean: a new approach, *Science*, **216**(4541), 11–19.

Gettens, R. J., 1951, The corrosion products of an ancient Chinese bronze, *Journal of Chemical Education*, **28**, 67–71.

Gettens, R. J., 1969, *The Freer Chinese Bronzes*, vol. 2*: Technical studies*, 127–31, Freer Gallery of Art, No. 7: Oriental Studies, Smithsonian Institution, Washington, DC.

Grolimund, D., Senn, M., Trottmann, M., Janousch, M., Bonhoure, I., Scheidegger, A. M., and Marcus, M., 2004, Shedding new light on historical metal samples using micro-focused synchrotron X-ray fluorescence and spectroscopy, *Spectrochimica Acta B*, **59**(10–11), 1627–35.

Harbottle, G., Gordon, B. M., and Jones, K. W., 1986, Use of synchrotron radiation in archaeometry, *Nuclear Instruments and Methods in Physics Research Series B*, **14**(1), 116–22.

Hargrove, S., 1997, *Technical observations and analyses of Chinese bronzes: ancient Chinese bronzes in the Saint Louis Art Museum*, 1–190, St Louis Art Museum, St Louis.

Hirao, Y., 2001, *Ancient East Asia: circulation of bronzes*, Tsuruyama Press, Tokyo.

Ikonnikov, A. B., 1975, *Mineral resources of China*, Geological Society of America, Washington, DC.

Janssens, K., Vittiglio, G., Deraedt, I., Aerts, A., Vekemans, B., Vincze, L., Wei, F., Deryck, I., Schalm, O., Adams, F., Rindby, A., Knochel, A., Simionovici, A., and Snigirev, A., 2000, Use of microscopic XRF for non-destructive analysis in art and archaeometry, *X-ray Spectrometry*, **29**, 73–91.

Jin, Z., 1991, Ore sources for bronze production in the Central Plain during the Late Shang Period, in *Proceedings of the 3rd International Symposium on the History of Science and Technology in China*.

Jin, Z., 2000, Scientific research on the bronzes of the Erlitou culture and exploration of the Xia civilization, *Wen Wu (Cultural Relics)*, **1**, 56–64, 69.

Jin, Z., Zheng, G., Hirao, Y., Hayakawa, Y., and Chase, W. T., 1998a, Lead isotope study of early Chinese bronze objects, in *The Fourth International Conference on the Beginning of the Use of Metals and Alloys (BUMA-IV)*.

Jin, Z., Chase, W. T., Hirao, Y., Yang, X., Mabuchi, H., and Miwa, K., 1998b, Lead isotope studies: some preliminary thoughts on the relationship between the bronze civilization in the Yellow River Valley and the Yangtze River Valley in Shang Dynasty, in *Proceedings of the International Symposium on the Shang Culture in Ancient China, Yanshi, Henan Province*.

Jin, Z., Chase, W. T., Hirao, Y., Zhao, D., Mabuchi, H., Miwa, K., and Chen, D., 1994, A study of the ratios of lead isotopes in bronzes from Shang tombs at Dayangzhou, Xingan, *Kaogu (Archaeology)*, **8**, 744–7 (in Chinese).

Jin, Z., Chase, W. T., Mabuchi, H., Miwa, K., Hirao, Y., Chen, D., and Zhao, D., 1998c, High radiogenic lead in Shang bronzes: a comparative study on the bronze wares from Sanxingdui site and those housed in the Sackler Museum, in *Proceedings of the International Conference on Chinese Archaeology Enters the Twenty-first Century*.

Jin, Z., Mabuchi, H., Chase, W. T., Chen, D., Miwa, K., Hirao, Y., and Zhao, D., 1995, A study on lead isotope ratios of the Sanxingdui pit burial bronzes, *Wen Wu (Cultural Relics)*, **465**(2), 80–5.

Linduff, K. M., Rubin, H., and Shuyun, S. (eds.), 2000, *The beginnings of metallurgy in China*, Chinese Studies, vol. 11, Edwin Mellen Press, Lewiston, NY/Queenston, Ontario.

Loewe, M., and Shaughnessy, E., 1999, *The Cambridge history of ancient China: from the origins of civilization to 221 BC*, Cambridge University Press, Cambridge.

Mabuchi, H., and Hirao, Y., 1987, Lead isotope ratios of lead ore deposits in East Asia, *Archaeology*, **73**(2), 71–117.

Mabuchi, H., Hirao, Y., and Nishida, M., 1985, Lead isotope approach to the understanding of early Japanese bronze culture, *Archaeometry*, **27**, 131–59.

McCann, L. I., Trentelman, K., Possley, T., and Golding, B., 1999, Corrosion of ancient Chinese bronze money trees studied by Raman microscopy, *Journal of Raman Spectroscopy*, **30**, 121–32.

Newbury, B. D., Notis, M. R., Stephenson, B., Cargill, G. S., and Stephenson, G. B., 2006, The astrolabe craftsmen of Lahore and early brass metallurgy, *Annals of Science*, **63**(2), 201–13.

Newbury, B., Stephenson, B., Almer, J. D., Notis, M., Cargill, G. S., Stephenson, G. B., and Haeffner, D. R., 2004, Synchrotron applications in archaeometallurgy: analysis of high zinc brass astrolabes, *Powder Diffraction*, **19**(1), 12–15.

Niederschlag, E., Pernicka, E., Seifert, T., and Bartelheim, M., 2003, The determination of lead isotope ratios by multiple collector ICP–MS: a case study of Early Bronze Age artefacts and their possible relation with ore deposits of the Erzgebirge, *Archaeometry*, **45**, 61–100.

Pantos, E., Kockelmann, W., Chapon, L. C., Lutterotti, L., Bennet, S. L., Tobin, M. J., Mosselmans, J. F. W., Pradell, T., Salvado, N., Buti, S., Garner, R., and Prag, A. J. N. W., 2005, Neutron and X-ray characterisation of the metallurgical properties of a 7th century BC Corinthian-type bronze helmet, *Nuclear Instruments and Methods in Physics Research B*, **239**(1–2), 16–26.

Pelton, A. D., 2006, Calculation and analysis of EpH diagrams related to the corrosion of Chinese bronzes, in *Report from THERMFACT LTD*, 1–39, Lehigh University, Quebec, Canada.

Peng, Z., Zhang, Z., He, J., Wang, Z., Liu, S., and Hua, J., 2000, Lead isotopic study of Shang Dynasty bronzes (13–11 B.C.) and their ore sources (in Chinese), *Nuclear Science and Techniques*, **11**(2).

Pernicka, E., Begemann, F., Schmitt-Strecker, S., and Grimanis, A. P., 1990, On the composition and provenance of metal artefacts from Poliochni on Lemnos, *Oxford Journal of Archaeology*, **9**(3), 263–98.

Pollard, A. M., and Heron, C., 2008, *Archaeological chemistry*, The Royal Society of Chemistry, Cambridge.

Rawson, J., 1990, *Western Zhou ritual bronzes from the Arthur M. Sackler Collections*, vol. 2A, Harvard University Press, Cambridge, MA.

Rawson, J., 2009, *Treasures from Shanghai—ancient Chinese bronzes and jades*, British Museum Press and the Shanghai Museum.

Robbiola, L., Blengino, J.-M., and Fiaud, C., 1998, Morphology and mechanisms of formation of natural patinas on archaeological Cu–Sn alloys, *Corrosion Science*, **40**(12), 2083–111.

Rosman, K. J. R., and Taylor, P. D. P., 1998, Isotopic compositions of the elements 1997, *Pure and Applied Chemistry*, **70**(1), 217–35.

Salvado, N., Buti, S., Tobin, M. J., Pantos, E., Prag, A. J. N. W., and Pradell, T., 2005, Advantages of the use of SR–FT–IR microscopy: applications to cultural heritage, *Analytical Chemistry*, **77**(11), 3444–51.

Schreiner, M., Fruhmann, B., Jembrih-Simburger, D., and Linke, R., 2003, X-rays in art and archaeology: an overview, *Powder Diffraction*, **19**(1), 3–11.

Scott, D. A., 2002, *Copper and bronze in art: corrosion, colorants, and conservation*, Los Angeles, Getty Publications.

Smith, C. S., 1981, *A search for structure: selected essays on science, art and history*, The MIT Press, Cambridge, MA.

Spoto, G., 2000, Secondary ion mass spectrometry in art and archaeology, *Thermochimica Acta*, **365**(1–2), 157–66.

Stephenson, G. B., Stephenson, B., and Haeffner, D. R., 2001, Investigations of astrolabe metallurgy using synchrotron radiation, *MRS Bulletin*, **26**(1), 19–23.

Stos-Gale, Z. A., Maliotis, G., Gale, N. H., and Annetts, N., 1997, Lead isotope characteristics of the Cyprus copper ore deposits applied to provenance studies of copper oxhide ingots, *Archaeometry*, **39**, 83–123.

Thorp, R. L., 2005, *China in the Early Bronze Age: Shang civilization*, University of Pennsylvania Press, Philadelphia, PA.

von Falkenhausen, L., 2006, *Chinese society in the age of Confucius (1000–250 BC): the archaeological evidence*, Los Angeles, Cotsen Institute of Archaeology, University of California.

Weeks, L., 1999, Lead isotope analyses from Tell Abraq, United Arab Emirates: new data regarding the 'tin problem' in western Asia, *Antiquity*, **73**, 49–64.

Xueqin, L., 2002, The Xia–Shang–Zhou Chronology Project: methodology and results, *Journal of East Asian Archaeology*, **4**(1–4), 321–33.

Yeung, C. S. L., Kwok, R. W. M., Lam, P. Y. K., Wong, S. P., Hark, S. K., Jin, Z., Wong, P. C. L., Yu, M. L., and Mark, K. K., 2000, SIMS analysis of lead isotope composition in ancient Chinese metallic artifacts, *Surface and Interface Analysis*, **29**(8), 487–91.

Young, M. L., Casadio, F., Schnepp, S., Almer, J. D., Haeffner, D. R., and Dunand, D. C., 2006, Synchrotron X-ray diffraction and imaging of ancient Chinese bronzes, *Applied Physics A—Materials Science & Processing*, **83**(2), 163–8.